A fast reconstruction algorithm for implementation of time-series DC optical tomography

Yaling Pei[a], Harry L. Graber[b], Randall L. Barbour[b]
[a]NIRx Medical Technologies LLC, 15 Cherry Lane, Glen Head, NY, USA 11545
[b]Department of Pathology, SUNY Downstate Medical Center,
450 Clarkson Avenue, Brooklyn, NY, USA 11203

ABSTRACT

A reconstruction technique that allows for real-time recovery of a time series of images is presented. The reconstruction technique is intended for use in a dynamic DC imaging system, and uses a model-based normalized-preconditioned-transformed system equation that considers light diffusion and is suitable for structures having arbitrary geometry and composition. The algorithm was tested on synthetic 2D media containing dynamic optical contrast features, with the presence of added noise and other uncertainties that commonly are present in experimental data. Post-reconstruction analyses performed on the reconstructed image time series show that the algorithm is capable of correctly locating the inclusions (total of eight) with excellent spatiotemporal accuracy, even in the presence of 32% noise and other uncertainties. In addition, a semi-analytic graphical tool we have identified, that can guide design of suitable measurement geometries and selection of appropriate refinement of the imaging operator, is described.

Keywords: Real-time imaging reconstruction, Time series analysis, Optical tomography

1. INTRODUCTION

A factor that can seriously limit the application domain of imaging techniques is the unavailability of analysis tools that can provide results within a time frame appropriate to the application. For instance, in cases where some form of interventional procedure is conducted it is important if not essential that imaging results be available in real time. Recently we have put forward the idea that, by virtue of its sensitivity to the hemoglobin signal, the method of diffuse optical tomography (DOT), when used to produce a time series of images, can represent a powerful functional imaging technique that is well suited to explorations of functional features of the vascular bed [1]. To this end, we have introduced working technology that is capable of collecting a continuous time series of tomographic measurements on a time scale sufficiently fast that the relevant properties of vascular dynamics are captured [2]. Characterization of these features in an imaging mode will require the availability of reconstruction techniques that are accurate as well as robust to the expected uncertainties of practical measurements. While this information could be made available in an off-line mode, it would be far more useful to generate the images as the detector data are being collected. This cannot be achieved by use of any of the inverse algorithms currently employed in the field of optical tomography, however, because of their computational burden and other difficulties. Thus, to further explore applications of functional diffuse optical tomography (fDOT) in imaging functional features of the vascular bed, it is crucial to develop a fast inverse algorithm for implementation of time-series optical tomography.

On a purely practical level, the availability of real-time imaging methods would also serve to render tractable the effort needed to explore fDOT data sets. To do so, however, will likely require some level of compromise between the goals of achieving the most quantitative imaging results possible and that of trading absolute accuracy (while useful dynamic information is retained) for data analysis speed. Our approach to this problem has been to consider analysis of relative measures based on the collection of DC data. In a series of reports we have demonstrated that our approach not only produces results that accurately locate contrast features in dense scattering media, but also that the temporal characteristics associated with these features can be recovered with remarkable fidelity [3-7]. Moreover, we have shown, by experiment, that the absorption contrast can be effectively isolated from scattering contrast [2,4]. We have also shown, with simulated data, that this capability is independent of the temporal behavior exhibited by the inclusions or their location in the medium, even in the limit where the absorption and scattering contrast are both spatially and temporally coincident [5].

In this report we have sought to extend our approach of analyzing relative measures to allow for the recovery of images in real time with a dynamic DC imaging system, by devising a normalized-preconditioned-transformed (NPD) inverse formulation (§2.1 – §2.3) and using truncated singular value decomposition (TSVD) to solve the inverse problem (§2.4). Accompanying the implementation of the algorithm, we have identified a semi-analytic graphical tool to guide design of suitable measurement geometries and selection of appropriate refinement of the imaging operator for image recovery. The proposed algorithm was tested on synthetic 2D media containing dynamic optical contrast features, along with additive noise and other uncertainties, including geometric size errors and source-detector position errors, which commonly are present in experimental data. Post-reconstruction analyses performed on the reconstructed image time series show that the algorithm is capable of correctly locating the inclusions with excellent spatiotemporal accuracy, even in the presence of 32% noise and the other uncertainties.

2. RECONSTRUCTION ALGORITHMS

2.1 Inverse formulation — the normalized difference method (NDM)

To clearly describe the problem under study, we denote the measurement data space and the reconstruction model space by $\mathbb{R}^M$ and $\mathbb{R}^N$, respectively. Usually $\mathbb{R}^M$ includes all the components for detector data acquisition, such as the image system and the measured target, while $\mathbb{R}^N$ includes the selected reference medium and geometry, the source-detector (SD) configuration, and the boundary conditions used for imaging reconstruction; here, M is the number of SD pairs in the set of measurements and N is the number of unknown parameters for the domain (geometry) to be modeled. When one optical property (e.g., absorption or diffusion coefficient) is considered, N is the number of the nodes of the mesh used to discretize the domain. When two optical properties are reconstructed, N is twice the number of the mesh nodes. Usually $M \neq N$. The reconstruction problem is overdetermined if $M > N$ and underdetermined if $M < N$.

From our previous work [3], time-series optical tomography based on the NDM can be described as

$$\mathbf{W}\,\delta\mathbf{x}^{(t)} = \delta\mathbf{u}^{(t)}, \tag{1}$$

where $\mathbf{W}$ is the $M\times N$ weight matrix for all time points (*i.e.*, $\mathbf{W}$ is not time-dependent), whose elements represent the fractional change in light intensity at each of the SD pairs on the surface resulting from an incremental change in each of the reconstructed optical properties associated with a discretized domain and a selected reference medium; $\boldsymbol{\delta}\mathbf{x}^{(t)} \in \mathbb{R}^N$ is a $1\times N$ vector of position-dependent unknown optical parameters at the t^{th} time point (t = 1, …, T), and represents the difference between one or more optical properties of the target and reference media; and $\boldsymbol{\delta}\mathbf{u}^{(t)} \in \mathbb{R}^M$ is a $1\times M$ vector of surface-measured detector readings at the t^{th} time point, and represents the normalized differences between two sets of measured data associated with the SD configuration. That is,

$$\left(\delta\mathbf{u}^{(t)}\right)_i = \left(\mathbf{r}^{(t)}\right)_i (\mathbf{u})_i, \qquad i = 1, 2, ..., M, \tag{2}$$

where $\mathbf{u}$ is a vector of computed detector readings corresponding to the selected reference medium for all time points, and $\mathbf{r}^{(t)}$ is a vector of the measured relative director data that has the form

$$\left(\mathbf{r}^{(t)}\right)_i = \frac{\left(\mathbf{u}_1^{(t)}\right)_i - \left(\mathbf{u}_2^{(t)}\right)_i}{\left(\mathbf{u}_2^{(t)}\right)_i}, \tag{3}$$

with $\mathbf{u}_2^{(t)}$ and $\mathbf{u}_1^{(t)}$ representing two sets of measured data at the t^{th} time point (typically, time-averaged mean *vs*. a specific time point). Thus we say that Eq. (1) describes a mapping procedure, in which vector $\boldsymbol{\delta}\mathbf{x}^{(t)}$ in model space $\mathbb{R}^N$ is mapped into vector $\boldsymbol{\delta}\mathbf{u}^{(t)}$ in data space $\mathbb{R}^M$ by means of the weight, or transformation, matrix $\mathbf{W}$.

2.2 Diagonal weighting preconditioning — row scaling

Row scaling pre-multiplies the weight matrix $\mathbf{W}$ and the data vector $\delta\mathbf{u}$ by a diagonal matrix $\mathbf{R}^{-1}$, and solves the normalized system

$$\mathbf{W}_R \delta\mathbf{x}^{(t)} = \delta\tilde{\mathbf{u}}_R^{(t)}, \tag{4}$$

where $\mathbf{W}_R = \mathbf{R}^{-1}\mathbf{W}$, $\delta\tilde{\mathbf{u}}_R^{(t)} = \mathbf{R}^{-1}\delta\mathbf{u}^{(t)}$, and the diagonal entries of $\mathbf{R}$ are the sums of the elements of the corresponding rows of $\mathbf{W}$ (i.e., $\left(\mathbf{R}\right)_{ii} = \sum_{j=1}^{N}\left(\mathbf{W}\right)_{ij}$, $\left(i = 1, 2, ..., M\right)$).

A row scaling technique usually is employed to improve the condition of the matrix. It has been observed that weight preconditioning with row scaling aids in detection of interior objects in the medium, and is especially critical to obtain fast and correct convergence when an iterative method such as conjugate gradient descent (CGD) is used, since the convergence rates of iterative methods greatly depend on the condition number of the matrix to be inverted.

2.3 Weight transformation — the least-squares solutions

To simplify, we represent any of the system equations shown in Eqs. (1) and (4) in the general form

$$\tilde{\mathbf{W}}\delta\tilde{\mathbf{x}}^{(t)} = \delta\tilde{\mathbf{u}}^{(t)}. \tag{5}$$

One common way to solve such a system in cases in which the equations are inconsistent (*i.e.*, no vector $\delta\tilde{\mathbf{x}}^{(t)}$ exists such that the left- and right-hand sides of Eq. (5) are exactly equal) is to look for a solution that minimizes the average error in the set of equations.

2.3.1 Overdetermined systems

In an overdetermined system there are more measurement data than unknowns in a system to be reconstructed (i.e., $M > N$), and the least-squares method leads to the minimization problem:

$$\min\left\{\left[\tilde{\mathbf{W}}\delta\tilde{\mathbf{x}}^{(t)} - \delta\tilde{\mathbf{u}}^{(t)}\right]^T\left[\tilde{\mathbf{W}}\delta\tilde{\mathbf{x}}^{(t)} - \delta\tilde{\mathbf{u}}^{(t)}\right]\right\}, \tag{6}$$

which gives rise to the system equation

$$\left[\tilde{\mathbf{W}}^{\mathrm{T}}\tilde{\mathbf{W}}\right]\delta\tilde{\mathbf{x}}^{(t)} = \tilde{\mathbf{W}}^{\mathrm{T}}\delta\tilde{\mathbf{u}}^{(t)}, \tag{7}$$

where $\tilde{\mathbf{W}}^{\mathrm{T}}$ is the transpose of $\tilde{\mathbf{W}}$. As a consequence, the least-squares solution of Eq. (5) for an overdetermined system is

$$\delta\tilde{\mathbf{x}}^{(t)} = \left[\tilde{\mathbf{W}}^{\mathrm{T}}\tilde{\mathbf{W}}\right]^{-1}\tilde{\mathbf{W}}^{\mathrm{T}}\delta\tilde{\mathbf{u}}^{(t)}. \tag{8}$$

Notice that the product appearing inside brackets in Eq. (8) is of size $N \times N$. Then $\tilde{\mathbf{W}}^{\mathrm{T}}\tilde{\mathbf{W}}$ is invertible if rank($\tilde{\mathbf{W}}^{\mathrm{T}}\tilde{\mathbf{W}}$) = N, and Eq. (7) has a unique exact solution (while, in this case, usually Eq. (5) has none).

2.3.2 Underdetermined systems

Most commonly, however, an optical tomography problem is severely underdetermined, because the affordable number of SD pairs, M, usually is substantially smaller than the number of unknowns, N, especially for 3D problems. Accordingly, an alternative derivation of the system equation is presented that yields a minimum-norm solution for this case [12]. By minimizing the squared vector of unknowns while enforcing the constraint $\tilde{\mathbf{W}}\delta\tilde{\mathbf{x}}^{(t)} = \delta\tilde{\mathbf{u}}^{(t)}$,

$$\min\left\{\left[\delta\tilde{\mathbf{x}}^{(t)}\right]^{\mathrm{T}}\delta\tilde{\mathbf{x}}^{(t)} + \left[\delta\tilde{\mathbf{u}}^{(t)} - \tilde{\mathbf{W}}\delta\tilde{\mathbf{x}}^{(t)}\right]^{\mathrm{T}}\boldsymbol{\gamma}^{(t)}\right\}, \tag{9}$$

where $\boldsymbol{\gamma}$ is a vector of Lagrange multipliers, taking the gradient of Eq. (9) with respect to $\delta\tilde{\mathbf{x}}^{(t)}$ and $\boldsymbol{\gamma}$, and setting the result equal to be zero yields

$$\delta\tilde{\mathbf{x}}^{(t)} - \tilde{\mathbf{W}}^{\mathrm{T}}\boldsymbol{\gamma}^{(t)} = \mathbf{0} \tag{10a}$$

and

$$\tilde{\mathbf{W}}\delta\tilde{\mathbf{x}}^{(t)} - \delta\tilde{\mathbf{u}}^{(t)} = \mathbf{0}. \tag{10b}$$

Substituting Eq. (10a) into Eq. (10b) gives

$$\tilde{\mathbf{W}}\tilde{\mathbf{W}}^{\mathrm{T}}\boldsymbol{\gamma}^{(t)} = \delta\tilde{\mathbf{u}}^{(t)} \tag{11}$$

The intermediate result is obtained by solving Eq. (11) is

$$\boldsymbol{\gamma}^{(t)} = \left[\tilde{\mathbf{W}}\tilde{\mathbf{W}}^{\mathrm{T}}\right]^{-1}\delta\tilde{\mathbf{u}}^{(t)}, \tag{12}$$

and substituting Eq. (12) into Eq. (10a) yields the final result,

$$\delta\tilde{\mathbf{x}}^{(t)} = \tilde{\mathbf{W}}^{\mathrm{T}}\left[\tilde{\mathbf{W}}\tilde{\mathbf{W}}^{T}\right]^{-1}\delta\tilde{\mathbf{u}}^{(t)}. \tag{13}$$

A solution similar to that in Eq. (13) for the underdetermined case can be derived by use of the weight transformation method proposed in [8].

Notice that the matrix product that appears inside the inversion of Eq. (13) or (14) is a $M\times M$ matrix. If M is small then so is the matrix to be inverted in Eq. (13), irrespective of the number of unknowns N, which opens the possibility of implementing real-time optical tomography, even for 3D problems.

2.4 SVD-based solutions

2.4.1 The singular value decomposition

By representing Eq. (7) or (12) in the general form

$$\mathbf{A}\mathbf{y}^{(t)} = \mathbf{b}^{(t)}, \qquad \mathbf{A}\in\mathbb{R}^{L\times L}, \tag{14}$$

where $L = N$ for a overdetermined problem and $L = M$ for a underdetermined one, we can write the singular value decomposition (SVD) of $\mathbf{A}$ as $\mathbf{A} = \mathbf{U}\boldsymbol{\Sigma}\mathbf{V}^{\mathrm{T}} = \sum_{i=1}^{L}\mathbf{u}_i\sigma_i\mathbf{v}_i^{\mathrm{T}}$, where $\mathbf{U} = (\mathbf{u}_1, \mathbf{u}_2,..., \mathbf{u}_L) \in \mathbb{R}^{L\times L}$ and $\mathbf{V} = (\mathbf{v}_1, \mathbf{v}_2,..., \mathbf{v}_L) \in \mathbb{R}^{L\times L}$ are matrices with orthnormal columns (*i.e.*, $\mathbf{U}^{\mathrm{T}}\mathbf{U} = \mathbf{V}^{\mathrm{T}}\mathbf{V} = \mathbf{I}_L$) and the diagonal matrix $\boldsymbol{\Sigma} = \mathrm{diag}(\sigma_{1,\ldots}\sigma_L)$ has nonnegative diagonal elements in nonincreasing order (*i.e.*, $\sigma_1 \geq \sigma_2 \geq \ldots \geq \sigma_L \geq 0$); the numbers σ_i are called the singular values of matrix $\mathbf{A}$, while vectors $\mathbf{u}_i$ and $\mathbf{v}_i$ are the left and right singular vectors of $\mathbf{A}$, respectively.

2.4.2 Truncated SVD (TSVD) solution

If we directly apply the above SVD to solve a linear system, i.e.,

$$\mathbf{y} = \sum_{\substack{i=1\\ \sigma_i\neq 0}}^{L}\frac{\mathbf{u}_i^{\mathrm{T}}\mathbf{b}}{\sigma_i}\mathbf{v}_i, \tag{15}$$

then small singular values tend to amplify noise in $\mathbf{y}$, resulting in bad reconstruction results. The truncated SVD (TSVD) approximates the ill-conditioned matrix $\mathbf{A}$ with the rank-k matrix $\mathbf{A}_k = \sum_{i=1}^{k}\mathbf{u}_i\sigma_i\mathbf{v}_i^{\mathrm{T}}$, $\sigma_i > \tau_{\mathrm{thr}}$, and leads to the TSVD solution:

$$\mathbf{y} \simeq \mathbf{y}_k = \sum_{i=1}^{k} \frac{\mathbf{u}_i^{\mathrm{T}}\mathbf{b}}{\sigma_i}\mathbf{v}_i, \qquad \sigma_k > \tau_{\mathrm{thr}}. \tag{16}$$

where τ_{thr} is a preset threshold. By means of truncation, the TSVD method produces a new problem with a well-conditioned rank-deficient matrix.

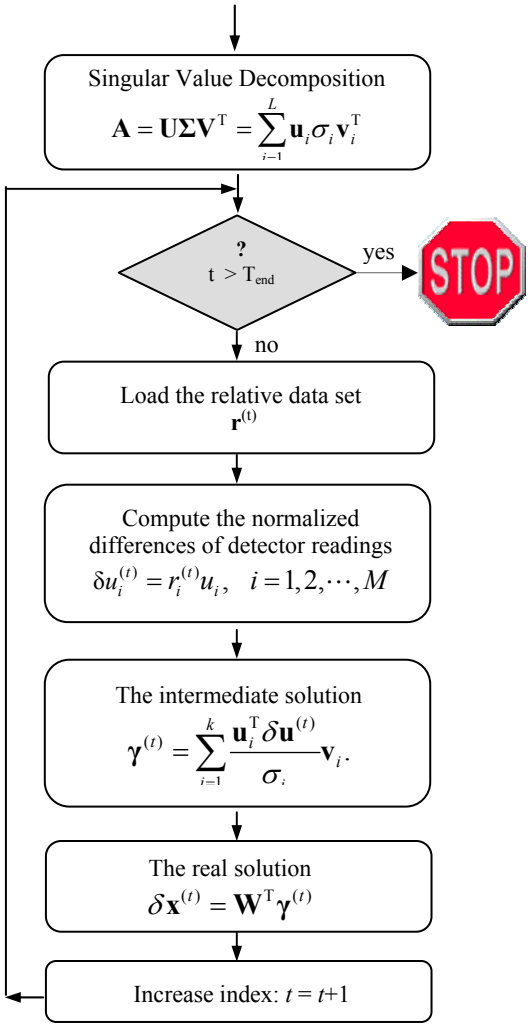

Figure. 1. Time-series optical tomography procedure.

2.5 Implementation of time-series optical tomography

Real-time dynamic DOT requires solving a series of time-dependent system equations having the same weight matrix but different detector reading vectors (i.e., in Eq. (5)). Therefore, minimizing overall computational cost is an important consideration, and one important aspect of this is to avoid as many duplicative computational processes as possible. At this time, SVD-based direct methods seem to be good choices for this purpose. Since we use the same reference medium to do image recovery for a time-series data set, the system matrix **A** is decomposed only at the first time point. Beyond that, the time-dependent intermediate solutions are sequentially calculated by implementing backsubstitution of TSVD with Eq. (16), replacing the right-hand side vector **b** each time. The time-series optical tomography procedure for a underdetermined case is described in Figure 1.

3. SIMULATION CONDITIONS

The computer-simulated dynamic phantom model examined here was the geometrically simple 2D circular object shown in Figure 2. The diameters of the model medium and of the embedded inclusions are 8 cm and 0.6 cm, respectively. The inclusions are grouped into four pairs marked by numbers 1 through 4, and are used to simulate the different dynamic tissues such as blood vessels.

The optical properties of the background medium were $\mu_a = 0.06$ cm^{-1}, $\mu_s' = 10$ cm^{-1}. The reduced scattering coefficient for the inclusions was the same as that of the background, and time-invariant. Absorption coefficients in the four pairs of inclusions varied by following four different aperiodic functions (i.e., $f_1(t), f_2(t), f_3(t)$ and $f_4(t)$) which are representative of complex temporal behaviors – quasiperiodic, chaotic, and stochastic – that have been reported as associated with vascular reactivity [5], to simulate time-dependent absorption contrast. The mean value $\overline{\mu}_a$ of the absorption is the same as the background absorption coefficient, and the instantaneous μ_a deviated from the mean value by at most 20%. Then the actual absorption coefficients for the four pairs of inclusion are represented as $\mu_a(i,t) = \overline{\mu}_a[1 + 0.2 f_i(t)]$, $i = 1, 2, 3, 4$. (See Ref. [5] for plots of $f_1(t) - f_4(t)$).

Computer-simulated time-series tomographic data for the simulated dynamic tissue model were acquired by using the finite element method to solve the diffusion equation with Dirichlet boundary conditions and a DC source. Forward-problem solutions were computed for each of sixteen sources positioned about the target at 22.5° intervals, with each source located at a depth of 2.5 mm inward from the extended boundary (i.e., within the strip lying between the physical

and extended boundaries). Intensity values at the sixteen source locations (only one of the sources was "on" during any one computation) were used as detector readings, leading to a total of 256 SD pairs. We also employed adaptive mesh techniques to produce more accurate FEM solutions during the data simulation process. The starting FEM mesh contained 789 nodes and 1488 elements, as shown in Figure 2(B). Time-series sets of detector readings for the simulated models were computed for each of 1000 time-varying optical coefficient values in the targets' inclusions. We denote the simulated time-series data set by $\mathbf{u}_{2D}^{(t)}$. The relative detector readings $\mathbf{r}_{2D}^{(t)}$ used for image recovery were generated by comparing individual elements in $\mathbf{u}_{2D}^{(t)}$ to the time-averaged mean values in $\bar{\mathbf{u}}_{2D} = T^{-1}\sum_{t=1}^{T}\mathbf{u}_{2D}^{(t)}$.

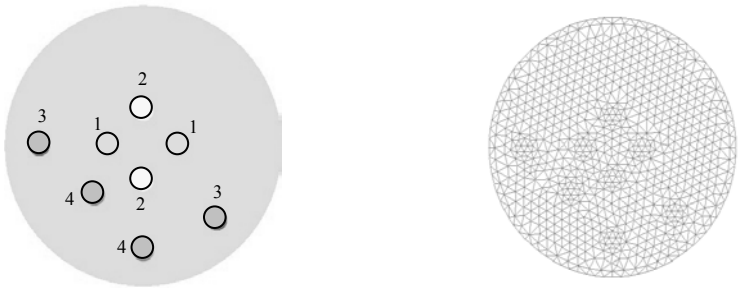

(A) Geometry (B) FEM Mesh

Figure 2. (A) Geometry of computer-simulated phantom models and, and (B) Starting FEM mesh used for adaptive FEM calculations to generate the computer-simulated time-series optical tomographic detector data.

Measurement noise was calculated based on the premise that the noise-to-signal ratio (*N*/*S*) was primarily a function of SD angle (*i.e.*, distance). We refer to the set of all SD pairs having the same central angle θ between the source and the detector as a "family." The noise-to-signal ratio with respect to θ was computed via the formula

$$N/S = K_0 + (K_{180} - K_0)(\theta/180)^{\alpha}, \tag{17}$$

where K_0 is the *N*/*S* at $\theta = 0^{\circ}$ (source and detector co-located; backscattering), K_{180} is the *N*/*S* at $\theta = 180^{\circ}$ (source and detector on opposite sides of the medium; transmission), and α is the exponent that defines the functional form of the *N*/*S*. Noise data generation proceeded by the following steps. We first computed the standard derivation of the Gaussian noise generator for each SD family by multiplication of the family mean value of detector reading $\mathbf{u}_{2D}^{(t)}(\theta)$ and the corresponding value of *N*/*S*. Next, at each time point we generated Gaussian noise samples $\mathbf{R}^{(t)}(\theta)$ associated with the SD families, and computed $\tilde{\mathbf{u}}_{2D}^{(t)}(\theta) = \mathbf{u}_{2D}^{(t)}(\theta) + \mathbf{R}^{(t)}(\theta)$. After the preceding operations were completed for all time points, we calculated the mean of the noise-added time-series data sets, $\bar{\tilde{\mathbf{u}}}_{2D} = T^{-1}\sum_{t}\tilde{\mathbf{u}}_{2D}^{(t)}$. Finally, relative time-series detector readings were computed based on the time-averaged mean values $\bar{\tilde{\mathbf{u}}}_{2D}$ of the noise-added data set $\tilde{\mathbf{u}}_{2D}^{(t)}$. For the current report, the parameters used to compute the random noise were K_0 = 0.01 (1%), α = 4, and K_{180} = 0.03 (3%), 0.05 (5%), 0.10 (10%), 0.15 (15%), 0.20 (20%), 0.25 (25%), 0.32 (32%), and 0.50 (50%).

In the presented simulation studies, we computed spatial maps of covariance (σ_{xy}) values between the four model functions and the recovered pixel time series, to assess the accuracy with which the recovered temporal behaviors coincide with the actual locations of the corresponding inclusions. The ideal result would be that the reconstructed $\mu_a(t)$ in pixels lying within the four paired inclusions, and only these pixels, will show significant covariance with model functions $\mu_a(1,t)$, $\mu_a(2,t)$, $\mu_a(3,t)$ and $\mu_a(4,t)$. The corresponding covariance images are

$$\mathbf{c}_i = \frac{\sum_{t=1}^{T}\mu_a(i,t)\mathbf{M}^{(t)} - T\bar{\mu}_i\bar{\mathbf{M}}}{T-1}, \qquad i = 1,2,3,4 \tag{18}$$

where $\mu_a(i,t)$ (i = 1,2,3,4) denotes the temporal fluctuations assigned to inclusions' absorption coefficients, and $\bar{\mu}_i$ is an estimate of $\mu_a(i,t)$ made by averaging over all time points; $\mathbf{M} = [\mathbf{M}^{(1)}\ \mathbf{M}^{(2)}\ \ldots\ \mathbf{M}^{(T)}]^{\mathrm{T}}$ is a $T \times N$ matrix that stores the reconstructed image time series, while $\mathbf{M}^{(t)}$ (t = 1,2, …, T) is the row of $\mathbf{M}$ which is the reconstructed image at the t^{th} time point, and $\bar{\mathbf{M}}$ denotes a temporal mean image.

4. SIMULATION RESULTS

In this section, computer-simulation results are presented based on the reconstruction algorithm and the model medium described in Sections 2 and 3. The space of parameters explored includes data noise, geometric size errors and uncertainty of SD positions. The influence of inaccurate reference medium properties are not explored here since the results associated with that type of error have been reported previously [3]. Accordingly, for all of the results reported in this paper, the optical properties of the reference medium selected are same as those of the background medium of the model, i.e., $\mu_a = 0.06\ \text{cm}^{-1}$, $\mu_s' = 10\ \text{cm}^{-1}$. The spatiotemporal accuracy of the proposed method is evaluated by computing the position-dependent temporal covariance maps derived from the set of reconstructed images and the model functions $\mu_a(1,t)$ through $\mu_a(4,t)$.

In our study, the corresponding reconstruction results have been computed by using different inverse formulations, such as normalized inverse formulation (i.e., Eq. (1) only), the normalized-transformed (NT) formulation (*i.e.*, Eq. (1) + weight transformation), the normalized-preconditioned (NP) formulation (*i.e.*, Eq. (1) + row scaling), and the NPD formulation (i.e., Eq. (1) + row scaling + weight transformation). However, only results obtained with the NPD formulation are presented, because of space limitations and because the performance of this reconstruction algorithm variant is superior to those of the other three in terms of accuracy, computational efficiency, or both. A more extensive comparison will be presented in a paper currently in preparation.

4.1 Effects of random data noise

Figure 3 shows the individual reconstructed images for the first eight time points and different levels of added noise generated by the method described in Section 3. For the noise-free case (first row), inspection shows that the spatial resolution of the individual images is strongly dependent on the values of optical properties in the medium. When the absorption perturbations are bidirectional (*i.e.*, negative and positive perturbations relative to the mean value of the optical properties are simultaneously present), such as at time points 1, 5, 6, 7 and 8, all of the inclusions located in the medium are well resolved. However, when the perturbations are monodirectional (i.e., only either negative or positive perturbations relative to the mean value of the optical properties are present), such as at time points 2 and 4, the inclusions located nearer the surface are well resolved but those located more deeply in the interior are not. For the noise-added cases, the results shows that the individual images quickly deteriorate into unrecognizability as the noise level increases. As we have recently emphasized and documented [1,5], improved resolution of the target medium can be obtained by post-processing the image-time series to extract different temporal measures of the system.

In Figure 4, we show spatial maps of the covariance between each of the assigned time functions and the image time series reconstructed from data sets with different levels of added noise. Inspection reveals that nearly complete isolation of each inclusion from the others is achieved, even up to 32% noise (i.e., $K_{180} = 0.32$).

4.3 Sensitivity to geometric size error

Uncertainties in target geometry (e.g., error in the estimate of the optical thickness of a tissue structure) may exist in practice. The effect of geometric size errors are examined by proportionally scaling the reconstruction mesh to levels 50% and 25% smaller than the correct diameter (i.e., 8 cm, which is the diameter of the forward-problem mesh), and to 25%, 50% and 75% larger than the true diameter. The temporal covariance maps for each of the four model functions and each resized mesh are shown in Figure 5. These results show that the reconstruction algorithm is robust to resizeable errors in the estimate of the object's size.

4.4 Effect of source-detector position error

Here we explore the sensitivity of the images to errors in the locations of the sources and detectors. The type of error considered here is modeled by adding normally distributed errors with standard deviations of up to 3˚ to the angular coordinates of the positions of the sources and detectors. Figure 6 shows covariance maps derived from the corresponding reconstructed image time series images. It is seen that the temporal model functions are separated and localized with considerable accuracy even at noise levels that have shown will significantly corrupt the quality of individual optical coefficient images.

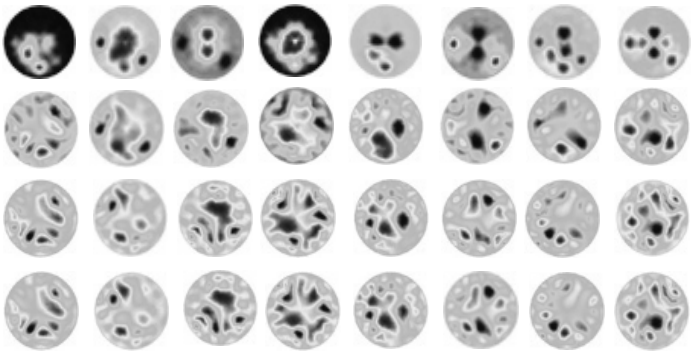

Figure 3. Time-series reconstruction results computed from the simulated data sets. The rows from top to bottom correspond to the data sets with 0, 3%, 10% and 32% added noise, respectively, while the columns from left to right correspond to time points 1 through time point 8, respectively.

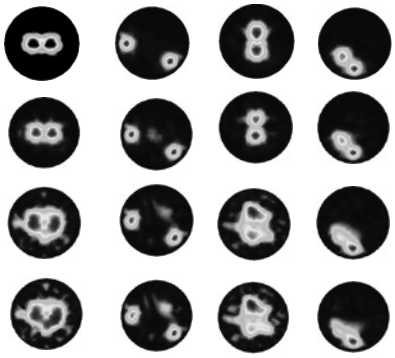

Figure 4. Spatial covariance maps for each of the assigned time-functions (columns) and the 2D image time series reconstructed from simulated data with 0, 3%, 10%, 32% added noise (rows), respectively.

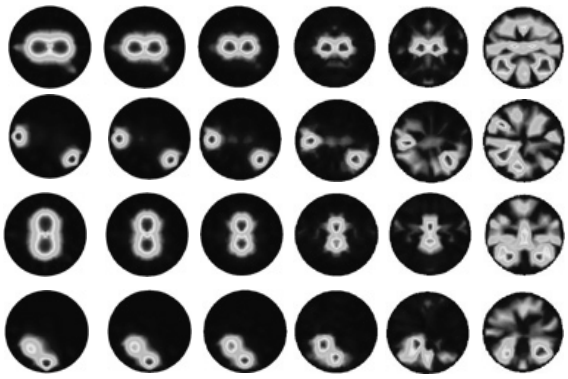

Figure 5. Spatial covariance maps for each of the assigned time-functions (rows) and the 2D image time series reconstructed from simulated data with different degrees of geometric size error. The rows correspond to time-functions chaos1, chaos2, quasiperiodic and stochastic, respectively, while the columns correspond to model radii 12cm, 10cm, 8cm, 6cm, 5cm and 4cm.

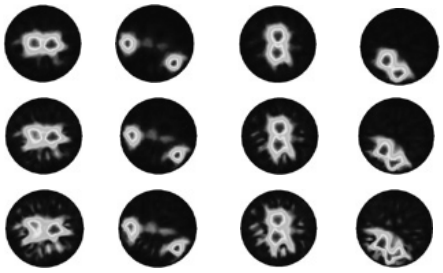

Figure 6. Spatial covariance maps for each of the assigned time-functions (columns) and the 2D image time series reconstructed from simulated data with source-detector position error. The columns correspond to time-functions chaos1, chaos2, quasiperiodic and stochastic, respectively, while the rows correspond to the source-detector positions having normally distributed errors with standard deviations of 1°, 2° and 3°, respectively.

4.5 Singular value analysis of weight matrix

The weight matrix, or image operator, that maps each set of detector readings into a set of medium optical properties contains information about both the reconstruction space (*i.e.*, reference medium for image reconstruction) and the measurement space (*i.e.*, measurement SD configuration). To better understand the nature of the weight matrix, we have developed the capability of drawing 2D maps of the columns of **U** and **V**, the left and right singular vectors of **W**, and of $\mathbf{U}_R$ and $\mathbf{V}_R$, the left and right singular vectors of $\mathbf{W}_R$. The columns of **V** and $\mathbf{V}_R$ are most informatively displayed in the same geometry as the reconstructed images, in which case they indicate the precise contribution of each pixel in the mesh used for solving the inverse problem to every singular vector. The columns of **U** and $\mathbf{U}_R$, on the other hand, are best displayed in a square geometry, where each row corresponds to a source and each column to a detector. The resulting maps indicate the precise contribution of each SD channel to every singular vector.

The first sixteen singular vectors (*i.e.*, those with the largest singular values) of the unscaled weight matrix **W** are shown in Figure 7(A), while the first sixteen singular vectors of the row-scaled weight matrix $\mathbf{W}_R$ are shown in Figure 7(B). These fractional views of the results of the SVD analysis demonstrates why row scaling of the weight matrix improves the accuracy of the reconstructed images and reduces the sensitivity of the NPD algorithm to additive noise. It is seen in Fig. 7(A) that the singular vectors corresponding to the largest singular values contain information from only one SD pair (top row), and from only a small group of pixels located close to the medium's surface (second row). Only with the seventeenth singular vector (not shown) do deeper-lying pixels even begin to contribute to the weight matrix. On the other hand, as seen in Fig. 7(B), deep-lying pixels contribute significantly to $\mathbf{W}_R$ even with the first singular vector. The significance of these results is that if a TSVD algorithm is used to solve the inverse problem, then a spatially accurate solution can be obtained with a smaller number of retained singular vectors if the weight matrix is row-scaled. Further, because the corrupting effects of additive noise tend to increase as the number of retained singular vectors increases, as a practical matter it may not be possible to reconstruct accurate images at all if the unscaled matrix **W** is used.

More generally, results such as those displayed in Figs. 7(A) and 7(B) show how this type of examination of the SVD of weight matrices can be used as a semi-analytic graphical tool to guide design of suitable measurement geometries and selection of appropriate reference medium and optimal regularization parameter for image reconstruction. That is, for any proposed distribution of source and detector locations, and/or any sort of pre-conditioning of the weight matrix, it can be determined in a straightforward manner whether all parts of the medium that investigators wish to examine will contribute significantly to the detector data. Another question that can be answered in this way is the signal-to-noise ratio that must be achieved in the measurement for successful recovery of the optical coefficients in all regions of interest.

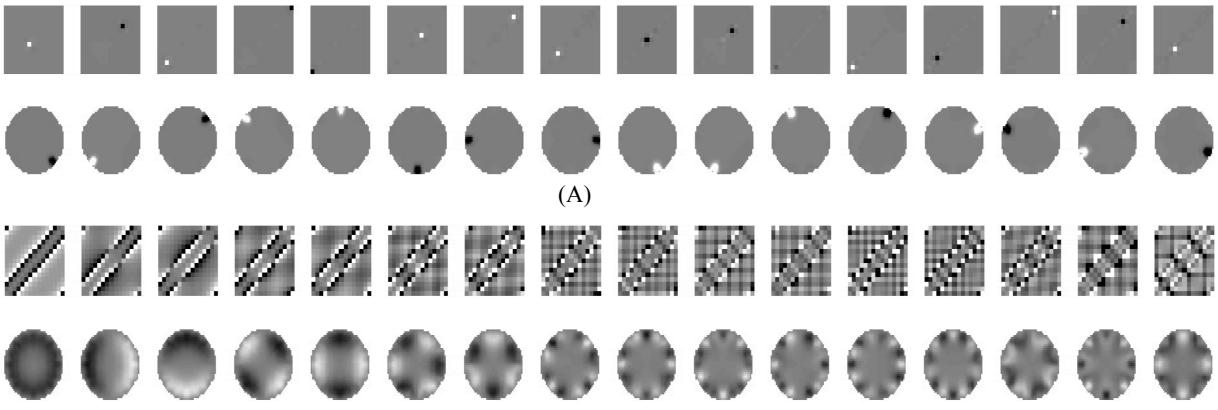

(A)

(B)

Figure 7. 2D maps of the first sixteen columns of **U** and **V**, the left and right singular vectors, of (A) weight matrix **W** and (B) row scaled weight matrix $\mathbf{W}_R$ used for the reconstructed images presented in this paper.

5. CONCLUSIONS

We have presented a fast reconstruction procedure for implementation of time-series DC optical tomography, using a normalized-preconditioned-transformed inverse formulation and truncated singular value decomposition. It has been shown that the developed algorithm is capable of correctly capturing dynamic fluctuations in medium absorption coefficients with excellent spatiotemporal accuracy, even in the presence of 32% noise and other uncertainties. Further advantages include simplification of system requirements, minimization of mismatch between the measure target and the mathematical model used for imaging recovery, and stabilization of the reconstructed images to inaccuracies in the selected reference medium.

In addition, the development of a semi-analytic graphical tool for SVD analysis of imaging operator provide a convenient way to guide selection of the optimal regularization parameter for implementation of image recovery and design of suitable measurement geometries for different tissue models.

6. ACKNOWLEDGEMENT

This research was supported in part by the US Army Medical Command (Contract No. DAMD17-03-0017, the New York State Department of Health, and by the National Institutes of Health under Grants R21-HL67387, R21-DK63692, R41-CA96102, and R43-CA91725.

7. REFERENCES

1. R. L. Barbour, H. L. Graber, Y. Pei, S. Zhong, C. H. Schmitz, "Optical tomographic imaging of dynamic features of dense-scattering media," *J. Optical Society of America A* **18**, 3018-3036 (2001).
2. C. H. Schmitz, M. Löcker, J. M. Lasker, A. H. Hielscher, R. L. Barbour, "Instrumentation for fast functional optical tomography," *Review of Scientific Instruments* **73**, 429-439 (2002).
3. Y. Pei, H. L. Graber, R. L. Barbour, "Influence of systematic errors in reference states on image quality and on stability of derived information for DC optical imaging," *Applied Optics* **40**, 5755-5769 (2001).
4. Y. Pei, H. L. Graber, and R. L. Barbour, "Normalized constraint algorithm for minimizing inter-parameter crosstalk in DC optical tomography," *Optics Express* **9**, 97-109 (2001).
5. H. L. Graber, Y. Pei, and R. L. Barbour, "Imaging of spatiotemporal coincident states by DC optical tomography," *IEEE Transactions on Medical Imaging* **21**, 852-866 (2002).
6. G. S. Landis, T. F. Panetta, S. B. Blattman, H. L. Graber, Y. Pei, C. H. Schmitz, R. L. Barbour, "Clinical applications of dynamic optical tomography in vascular disease," in *Optical Tomography and Spectroscopy of Tissue IV (Proceedings of SPIE, Vol. 4250)*, B. Chance, R. R. Alfano, B. J. Tromberg, M. Tamura, E. M. Sevick-Muraca, Eds., pp. 130-141 (2001).
7. C. H. Schmitz, H. L. Graber, H. Luo, I. Arif, J. Hira, Y. Pei, A. Bluestone, S. Zhong, R. Andronica, I. Soller, N. Ramirez, S.-L. S. Barbour, R. L. Barbour, "Instrumentation and calibration protocol for imaging dynamic features in dense-scattering media by optical tomography," *Applied Optics*, Vol. 39, pp. 6466-6486 (2000).
8. E. Y. Lin, Y. Wang, Y. Pei, R. L. Barbour, "Solution of the Perturbation Equation in Optical Tomography Using Weight Functions as a Transform Basis" in *Advances in Optical Imaging and Photon Migration (OSA Trends in Optics and Photonics, Vol. XXI)*, J. G. Fujimoto, M. S. Patterson, Eds., (Optical Society of America, Washington, DC, 1998) pp. 197-202.